ScienceDirect®

Ferroelectric composite-based piezoelectric energy harvester for self-powered detection of obstructive sleep

Swati Panda [a], Hyoju Shin [a], Sugato Hajra [a], Yumi Oh [a], Wonjeong Oh [a], Jeonghyeon Lee [a], P.M. Rajaitha [a], Basanta Kumar Panigrahi [b], Jyoti Shukla [c], Alok Kumar Sahu [d], Perumal Alagarsamy [d], Hoe Joon Kim [a e] ⊠

[a] Department of Robotics and Mechatronics Engineering, Daegu Gyeongbuk Institute of Science and Technology (DGIST), Daegu, 42988, South Korea

[b] Department of Electrical Engineering, Siksha 'O' Anusandhan University, Bhubaneswar, 751030, India

[c] Department of Electrical Engineering, Poornima College of Engineering, Jaipur, 303903, India

[d] Department of Physics, Indian Institute of Technology- Guwahati, Assam, 781039, India

[e] Robotics and Mechatronics Research Center, Daegu Gyeongbuk Institute of Science and Technology (DGIST), Daegu, 42988, South Korea

? What do these dates mean?

Check for updates

Show less ∧

☰ Outline | ⁂ Share | 🇔 Cite

Get rights and content ↗

Referred to by   Comment on "Ferroelectric composite-based piezoelectric energy harvester for self-powered detection of obstructive sleep"

Journal of Materiomics, Volume 10, Issue 5, September 2024, Pages 1144-1146

Alexander Tkach, Olena Okhay

📄 View PDF

Highlights

- Lead free ferroelectric ceramics were synthesized by ceramic technology.

- PENG delivered voltage, current, and power density of 25 V, 92 nA, and 0.64 μW.

- Biomechanical energy harvesting from daily human activities.

- Detection of obstructive sleep disorder using self-powered systems and CNN.

Abstract

Lead-free piezoelectric ceramic is a promising material for energy harvesters, as they have superior electromechanical, ferroelectric, and piezoelectric properties. In addition, piezoelectric ceramics can be blended with polymer to achieve high-flexibility polymer-ceramic composites, providing mechanical robustness and stability. In this context, a new lead-free ferroelectric material, having the chemical formula $SrTi_2O_5$ (STO), was synthesized using a high-temperature solid-state reaction. Detailed analyses of the structural, morphological, and electrical properties of the synthesized material were performed. STO crystallizes with orthorhombic symmetry and space group of $Cmm2$. The frequency and temperature-dependent dielectric parameters were evaluated, and impedance spectroscopy shed light on the charge dynamics. The PDMS-STO composites at different mass fraction of the STO were prepared using a solvent casting route, and a corresponding piezoelectric nanogenerator (PENG) was developed. The electrical output of the different PENG by varying massfractions of STO in PDMS and varying force were investigated. The 15% (in mass) PENG device delivered the highest peak-to-peak voltage, current, and power density of 25 V, 92 nA, and 0.64 μW @ 500 MΩ, respectively. The biomechanical energy harvesting using the PENG device by daily human motions, bending of the device, and attaching the device to laboratory equipment was demonstrated. Later the PENG device was attached to the human throat region, and snoring signals were recorded. A classification model was designed employing the convolutional neural network (CNN) model. Efforts have been laid to differentiate between normal and abnormal snores, which could help the patient with screening and early disease detection, contributing to self-powered healthcare applications.

Graphical abstract
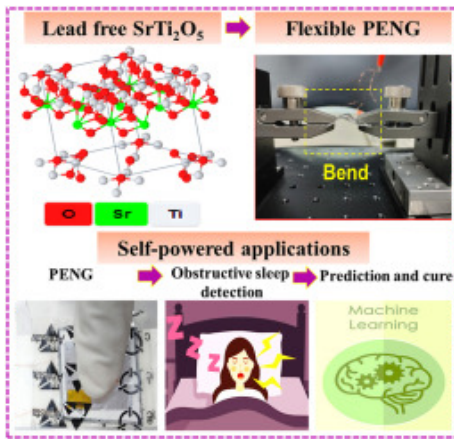
Download: Download high-res image (335KB)

Download: Download full-size image

Keywords

Lead-free; Ferroelectric; Nanogenerator; Sleep disorder

---

1. Introduction

A common respiratory disease associated with sleep called obstructive sleep apnea (OSA) can have terrible consequences [1,2]. According to estimates, 936 million adults between the ages of 30–69 have moderate to severe OSA, which can also cause additional health issues like ischemic stroke, coronary heart disease, angina pectoris, and poor sleep habits. It may also result in elevated blood pressure, pulmonary edema, and irregular heartbeats, which can result in premature death [3]. As a result, we must closely monitor OSA symptoms as they appear. More than 80% of OSA sufferers report snoring as their most prevalent and early symptom [4]. The narrow oropharynx of the upper airway (UA) causes turbulent airflow, which can cause soft tissues to vibrate and produce snoring. Based on the size and shape of the UA, different snoring patterns with different sounds or frequencies are produced. As a result, the snoring frequencies of signals produced by respiratory distress and mild snorers may vary [5]. It can be identified by a temporary pause of breathing accompanied by a complete restriction of the UA, despite continued abdomen and chest wall motions [6]. Overnight multi-channel polysomnography (PSG) is the standard method for diagnosing OSA, which could be labor and time-intensive to set up and analyze [7]. The proper medical procedures may require specific assistance at the test site and are also not a cost-effective technology. Hence a possible alternative is to diagnose OSA more quickly and cost-effectively by analyzing the signal of snore generated by the PENG during normal and abnormal snoring events. In this study, Convolutional Neural Network (CNN) and Gramian Angular Summation Field (GASF) techniques are used to predict the accuracy and efficiency of snoring patterns.

Wearable electronic devices have become of great public interest since the 1990s, aiming to provide users with a way to manage their health problems and take clinician help quickly to recover [8]. To

sense, analyze, and transmit data continuously, these wearables depend on a continuous power source such as a battery [9,10]. The battery suffers several demerits, such as low lifetime, less accessibility, and environmental pollution [11]. Unlike solar or wind, kinetic energy sources are not dependent on time and location [12]. Energy can be harvested by employing one or a combination of transduction mechanisms such as electromagnetic, triboelectric, and piezoelectric [[13], [14], [15], [16], [17]]. The piezoelectric energy harvesting mechanism uses a piezoelectric material that can directly convert mechanical vibrations into electrical energy [18,19]. Therefore, their device design is easily integrated with wearables and sensitive to small displacements/vibrations.

Industries and research groups widely use piezoelectric materials such as lead zirconate titanate (PZT) [20,21]. However, such types of lead-based materials are bar shortly by future electronics development owing to their toxicity and adverse effect on ecology [22]. In this context, finding an alternative material with superior electromechanical and high piezoelectric properties is the need of the hour. Lead-free materials are a possible candidate for piezoelectric energy harvesters as they are chemically stable, have tunable properties, and can be applied to use as capacitors, sensors, or memory devices [[23], [24], [25]]. STO comes from the Sr—Ti—O compound class. In this class, $SrTiO_3$ is widely investigated, having a cubic symmetry and space group: $Pm3m$ [26]. This system has a colossal dielectric constant, low leakage current, and high tunability. According to the material project datasheet, Panda $etal$. suggested that the new titanate system STO crystallizes in the orthorhombic symmetry having space group $Cmm2$ corresponding to a polar space group. They also claim ferroelectric properties exist in materials with polar space groups [27]. In this context, TiO_2-modified $SrTiO_3$ as a new ferroelectric system is investigated, and flexible polymer-ceramic composites act as a base for PENG design. STO comprises unidentical Sr^{2+} and Ti^{4+} sites. The distortion of TiO_6 octahedra and TiO_5 trigonal bipyramids leads to the origin of ferroelectricity in STO [28]. The STO structure is similar to the $BaTi_2O_5$, which also shows ferroelectricity from Ti^{+4} ions displacement and is thermodynamically originating in the temperature range between (1 220–1 230°C) as a metastable phase [29,30]. Fisher $etal$. have also reported that $SrTi_2O_5$ patterns, such as perovskite-derived structures with intermixing of the Sr and Ti cations on (001) planes, should exhibit loss of symmetry and greatly reduced intensity in diffraction scans for the (001) and (003) perovskite peaks. More research is needed to pinpoint the exact structural incorporation mechanism in $SrTi_2O_5$ film [31]. Hence, STO can act as a promising piezoelectric material for widespread applications. Flexibility is an important consideration in mechanical energy harvesters since it allows for a wide range of applicability to actualize a body-mountable energy harvester. Previously, it was shown that composite-based materials work well in mechanical energy harvesting [32,33]. Polydimethylsiloxane (PDMS) is frequently employed as a host polymer to build a piezoelectric composite owning to its low Young's modulus, appropriate biocompatibility, outstanding transparency, cost-effectiveness, strong thermal and chemical durability [34,35]. TableS1 compares state-of-the-art PDMS-ceramics composites based on PENG and the present study.

In this work, a new class of ferroelectric material STO was synthesized with the correlation of several dielectric, ferroelectric and structural properties. The polymer-ceramic composites with different mass fraction of STO in PDMS were used in designing PENG. The various electrical response of the PENG devices was evaluated to optimize the best composition. The charging of the capacitors and biomechanical energy harvesting of the PENG device was demonstrated to showcase the importance of PENG as a reliable energy scavenger. The computational approach was used to differentiate the various type of snoring patterns and evaluate the accuracy of the PENG device. Such self-powered

and battery-free sleep monitoring units can benefit patients by recognizing and treating their problems to ensure good health.

2. Experimental

STO particles were synthesized using a solid-state reaction route. At first, proper amounts of high-purity starting oxides and carbonates, such as strontium carbonate and titanium oxide, were mixed using wet grinding in an agate mortar pestle. Then the consistently mixed powder was moved to an alumina crucible inside a muffle furnace. The calcination temperature of 900°C for 5h was programmed. After that, the fine particles of STO were obtained. To measure the dielectric and impedance properties, disc shape pellets were fabricated. The powder was mixed with organic binder polyvinyl alcohol, and cold pressure was applied using a hydraulic press, converting the powder into a pellet shape. The pellets were kept in an alumina tray and placed inside the furnace, where the sintering was carried out at an elevated temperature of 1 000°C for 5h. The sintered pellet was painted with silver paste on the opposite side and directly utilized to measure electrical properties.

The STO particles were mixed with polydimethylsiloxane (PDMS) to form polymer-ceramic composites. The PDMS was mixed in a ratio of 10:1 (monomer: hardener) and stirred using a glass rod for 10min. Then different mass fraction of the STO particles were mixed carefully, and stirring continued. After the powder and polymer are mixed homogenously, it was cast upon a glass Petri plate. Further, it was transferred into a vacuum oven and kept at 70°C for 5h to dry. Then a flexible free-standing PDMS-STO composite was obtained. For making PENG, the composite film was cut into 3cm×3cm, and aluminum foil electrodes of 2cm×2cm were attached. The copper wires were connected to the aluminum using the silver paste, and finally, the device was encapsulated using an antistatic tape. Further, the poling of all fabricated PENG devices was carried out by a high-voltage DC poling unit under 2kV for 1h.

The structural information about the STO sample was traced using a powder X-Ray Diffractometer (M/S Panalytical Empyrean, Netherlands) having Cu-K$_\alpha$ radiation and a step size of 2° per minute. The X-ray tomography beamline imaging was performed at the Synchrotron Light Research Institute (SLRI) in Nakhon Ratchasima, Thailand. A 2.2-T multipole wiggler in the Siam Photon Source operated at 1.2GV generated synchrotron radiation X-rays from a filtered polychromatic beam at an energy of 11.5kV and 32m, and source-to-sample distance was kept unchanged. Drishti software was utilized to render 3D representations of the tomographic volumes of the composites.

The surface morphology of composite and powder was obtained using a scanning electron microscope (M/S SU-8230 Hitachi, Japan), and composition was quantified by an EDS detector manufactured by Oxford Instruments. The Raman modes were traced at room temperature using a Raman spectrometer (M/S Renishaw inVia Qontor, UK) at 633nm excitation wavelength. The hysteresis loop was recorded at room temperature using a ferroelectric loop tester (M/S Marine India). An impedance analyzer (M/S Hioki IM3470, Japan) measured the electrical properties of the samples at a wide range of frequencies and temperatures. A programmable linear motor (M/S LinMot, USA) applied periodic forces to a PENG device. The PENG output was recorded using an electrometer (M/S Keithley, USA) and a lab view program. Computer software such as Matlab R2018a and Python 3.7 analyzed the snoring and framing of CNN.

3. Results and discussion

Fig. 1 depicts the synthesis approaches of STO particles formed by the solid-state route at high temperatures (a). The mixture was then combined with PDMS polymer, using a PDMS ratio of monomer: hardener (10:1). After homogeneous mixing, it was placed onto a glass Petri dish and dried for 5h at 70°C in a convection oven. The PDMS-STO composites' flexible, free-standing film was later employed to make energy harvesters. The composite film is extremely rollable, flexible, and stretchable, as shown in Fig. 1(b). The PENG device's operation is depicted in Fig. 1(c), where there are three conditions: (i) initial, (ii) with force, and (iii) without force. The poling mechanism assisted dipoles in orienting themselves in the direction of an applied field. There is no formation of electrical output in the initial state since the device remain in an equilibrium state. As by applying the vertical compressive force is applied in to PENG, a compressive strain causes total polarization of the composite, resulting in a piezoelectric potential between the top and bottom electrodes. External free charges will move and accumulate at the electrodes to screen the piezoelectric potential. During this process, an output signal from the PENG can be detected. When the vertical mechanical force is removed, the vertical strain and piezoelectric potential between the two electrodes of PENG slowly vanish. The accumulated charges travel in the opposite direction, producing a negative electric signal. Due to the good elasticity of the PDMS matrix, a small tensile strain will be produced after the first return to the original state, resulting in a reverse piezoelectric potential. As previously stated, output pulse signals from the PENG device were obtained while the external compressive force was continuously applied and released.
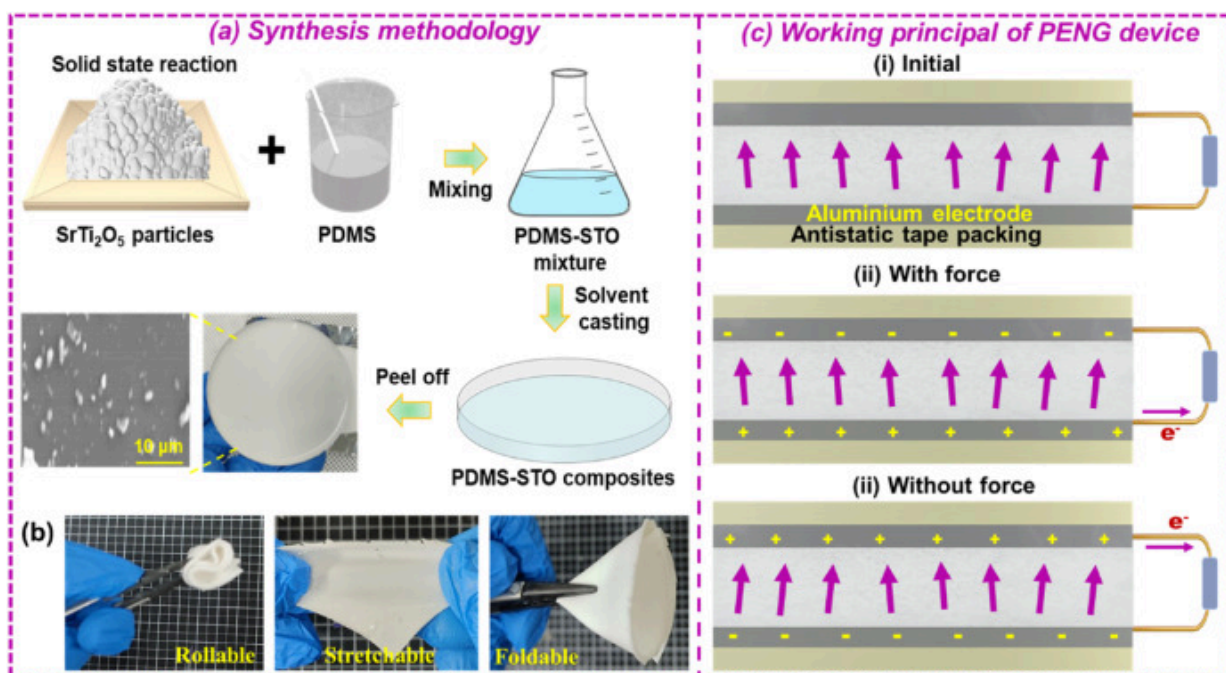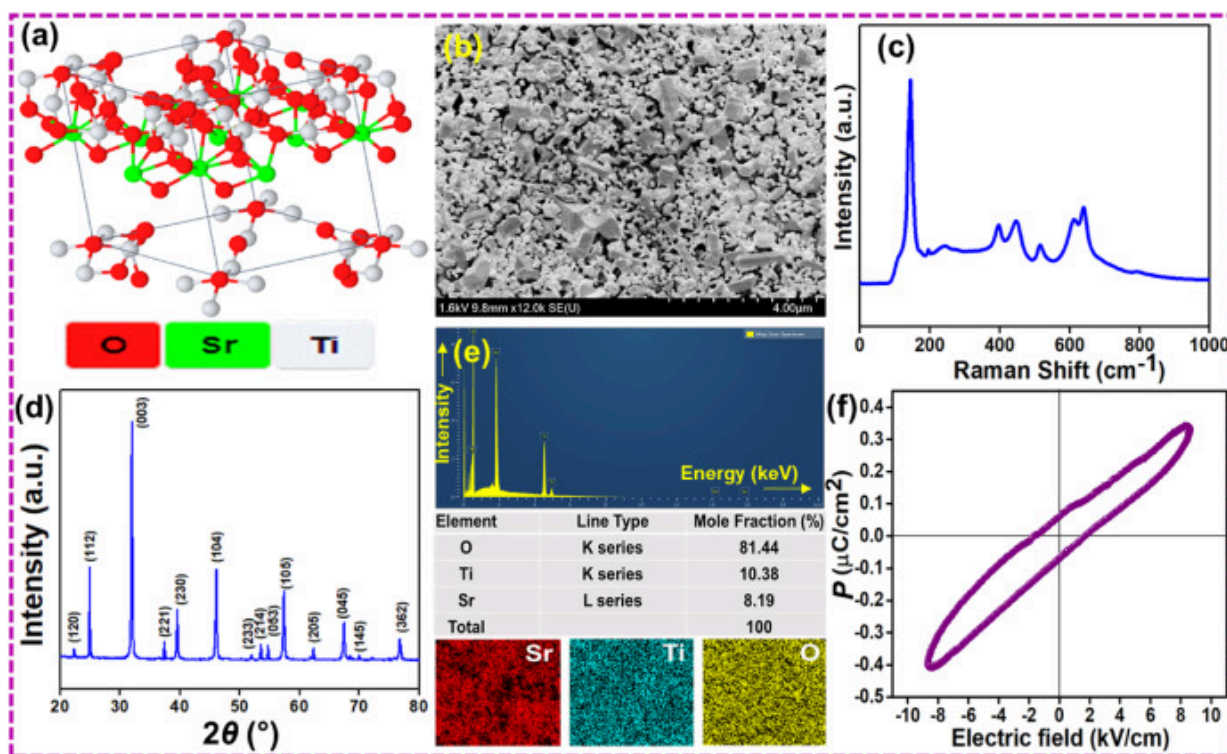

Download: Download high-res image (791KB)

Download: Download full-size image

Fig. 1. **Synthesis route.** (a) synthesis methodology of polymer ceramic (PDMS-STO) composites; (b) digital image of composite film showing high flexibility, stretchability, and rollable features and (c) working mechanism of PDMS-STO composite-based PENG device.

Fig. 2(a) displays the molecular structure of the prepared STO material constructed using VESTA software and the. CIF file was obtained from crystal structure library "The materials Project". The

surface morphology of the prepared STO was characterized using FESEM and shown in Fig.2(b). The morphology reveals an irregular and significantly random size distribution of particles. Fig.S2 shows the X-ray tomographic image of the PDMS-STO composites showing a uniform distribution of the STO particles over the PDMS matrix. To confirm the chemical structure and the structural distortion in the presently investigated STO sample, the Raman spectrum was obtained in the spectral range of 10–$1\,000\,cm^{-1}$ and displayed in Fig.2(c). It can be seen that the Raman spectrum exhibits nine bands at 107, 144, 195, 239*, 401, 447, 515, 612*, 639 and $797\,cm^{-1}$. Among these, the Raman bands at 144, 195, 239, 401, 447, 515, 612, 640 and $797\,cm^{-1}$ confirm the presence of the Ti^{4+} state in the STO sample. The orthorhombic space group of STO is expected to crystallize in TiO_2SrTiO_3 form such that there are three Ti^{4+} sites: (i) in the first Ti^{4+} site, Ti^{4+} is expected to bond with six O^{2-} atoms to form distorted TiO_6 octahedra, (ii) Similarly, the Ti^{4+} site bonds in a five-coordinate geometry to five number of O^{2-} atoms in the second Ti^{4+} site, and finally (iii) Ti^{4+} is also bonded to five O^{2-} atoms to form the structure of distorted TiO_5 trigonal bipyramids in the third Ti^{4+} site [27]. On the other hand, Raman bands at 107, 171, 239* and 612* cm^{-1} reveal the presence of the Sr^{2+} state in the sample [[36], [37], [38]]. As with Ti^{4+}, Sr^{2+} is also expected to be in 3 sites: (i) Sr^{2+} bonds with four O^{2-} atoms, six O^{2-} atoms, and eight O^{2-} atoms in the first, second and third sites of Sr^{2+} in the respective coordinate geometries. These observations agree with the structural information obtained from the XRD results, confirming the formation of the $SrTi_2O_5$ structure in the studied STO sample.

Download: Download high-res image (1MB)
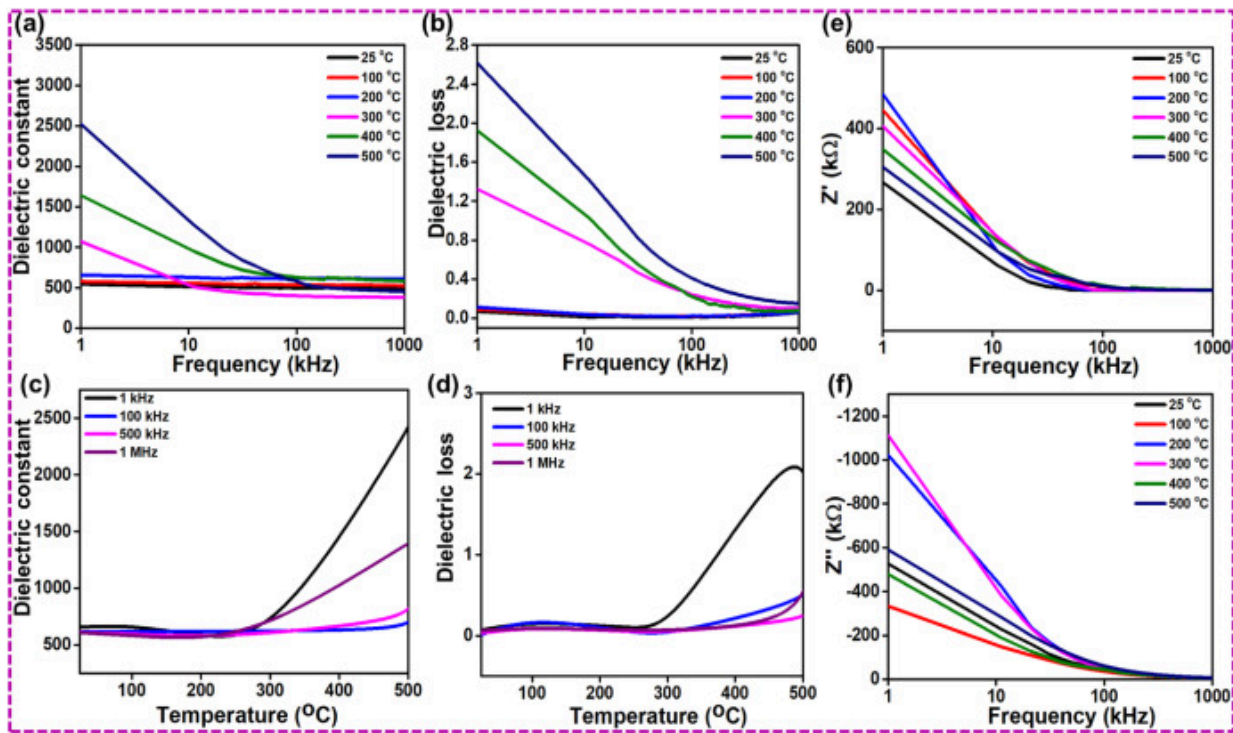
Download: Download full-size image

Fig.2. **Physio-chemical properties of STO.** (a) Molecular structure; (b) Surface morphology; (c) Raman spectra; (d) XRD pattern; (e) EDS spectra, mole fraction of each element and elemental color mapping and (f) *P-E* loop of the STO sample.

The X-ray diffraction (XRD) pattern was obtained to understand the crystal structure of the prepared STO sample, as shown in Fig.2(d). The acquired XRD pattern was compared with the XRD patterns of TiO_2 and $SrTiO_3$ individually (not shown here), and it is found that there are no exact matches with

the individual phases of TiO_2 and $SrTiO_3$ [[39], [40], [41]]. Hence, it is believed that the STO sample exhibits a new class of material with the possible structure of $SrTi_2O_5$, *i.e.*, TiO_2SrTiO_3, called polycrystalline orthorhombic structure having a space group of *Cmm*2 (35), as reported by Panda *etal.* [27]. Limited references are available in this new material; thus, the obtained XRD pattern can be compared only with the study reported by Panda *etal.* A detailed study using various structural and microstructural analyses is the main scope of future work. The POWD-MULT software was utilized to check the experimental pattern with different symmetry, and finally, it matched well with the orthorhombic phase. The lattice parameters are found to be $a=b=9.11$Å and $c=11.55$Å.

To study the presence of any impurity elements/phases and to confirm the uniformity of the elements present, the EDS analysis of the STO sample was investigated and presented in Fig.2(e). It can be seen that all elements are quite similar to the base composition without the presence of any impurity. Further, the EDS elemental mapping noticeably shows the highly homogeneous distribution of Sr, Ti and O elements, confirming the formation of STO without any impurity phases, even down to a smaller regime. Fig.2(f) shows the ferroelectric behavior of STO. The *P-E* loop of the STO at room temperature shows a remnant polarization of $0.07\mu C/cm^2$. It is well known that all ferroelectric materials are piezoelectric. Hence STO material can be a good candidate for designing PENG. The *P-E* loop of the PDMS and PDMS-STO 15% composite is shown in Fig.S3. Due to the STO particles in the PDMS, there is a notable amplification of internal polarization in the composite.

Fig.3(a-b) shows the frequency-dependent dielectric constant and dielectric loss of the STO material at various temperatures. At low frequencies, the dielectric constant increases, which can be attributed to the activation of all polarization in that region, while the loss factor rise is attributed to the dominance of DC conductivity [42,43]. As the frequency increases for all temperatures, the loss and dielectric constant value decrease. The inertial effect of the dipoles and reduction of space charge polarization at higher frequencies could reduce the dielectric constant. At higher frequencies, the variation of an electric field is rapidly changing, so the dipoles cannot follow it, leading to a decrease in the dielectric constant value [44,45]. Fig.3(c and d) shows the temperature-dependent dielectric constant and loss at various frequencies. The temperature-dependent dielectric constant is useful to shed light on the curie temperature of the material. However, it can be observed that with the rise in temperature at various frequencies, the value of the dielectric constant keeps on rising. It can be said that the Curie temperature or phase transition temperature lies well above the experimental temperature range of 500°C. The increased loss factor in the higher temperature region may be due to the thermally activated charge carriers that take part in the conduction process and increase dielectric loss [46]. The relative permittivity of the PDMS matrix ($\varepsilon_{pdms}=3$) can be improved by incorporating piezoelectric particles (STO) having high relative permittivity ($\varepsilon_{STO}=550$) at room temperature. Fig.S4 shows the frequency-dependent dielectric constant of PDMS and PDMS-STO15% (in mass, the same below) at room temperature.

Fig.3. **Electrical properties of STO.** (a–b) Frequency-dependent dielectric constant and dielectric loss at different temperatures; (c–d) Temperature-dependent dielectric constant and dielectric loss at different frequencies and (e–f) Frequency-dependent real-imaginary part of impedance at different temperatures of the STO sample.

Further, 2%, 5%, 10%, 15% and 20% STO particles were blended in the PDMS matrix to form the composites. The corresponding effective permittivity (ε_{eff}) of the composites is expressed as $\varepsilon_{eff} = \varepsilon_{pdms} f_{pdms} + \varepsilon_{STO} f_{STO}$. f_{pdms} and f_{piezo} correspond to volume fractions of the PDMS matrix and STO particles, respectively. According to fundamental piezoelectric theory, the piezoelectric coefficient (d_{33}) of composite films can be assessed using the piezoelectric voltage constant (g_{33}) and the effective relative permittivity (ε_{eff}) of the composite film [47]. The relationship can be given by $d_{33} = g_{33} \times (\varepsilon_0 \varepsilon_{eff})$. Hence the dielectric properties are directly correlated to the piezoelectric properties of the material. The voltage output of the PENG is directly related to the relative permittivity and piezoelectric coefficient given by $V_{oc} = g_{33} \sigma Y t$ where the piezoelectric voltage constant is g_{33}, Y is Young's modulus of composite, t is the thickness of the material, σ is the strain in the perpendicular direction. The frequency-dependent real and imaginary part of the impedance at various temperatures is shown in Fig.3(e-f). From the real part of the impedance, as the temperature increases, the value of Z' first increases and then decreases, confirming that there is a contribution of both negative and positive temperature coefficient resistance in the STO. The imaginary part of impedance Z'' versus frequency depicts the non-Debye relaxation nature of the STO sample.

The PENG was fabricated by utilizing various composites 2%STO-PDMS (PSTO2), 5%STO-PDMS (PSTO5), 10%STO-PDMS (PSTO10), 15%STO-PDMS (PSTO15) and 20%STO-PDMS (PSTO20) respectively. Fig.4(a-b) shows the voltage and current of different PENG devices at different mass fraction. The voltage and current output value are enhanced until PSTO15 and then decrease. It can be noted that increasing 20% STO into PDMS lead to particle agglomeration, causing the decline in output as force

cannot be distributed properly to the composites. Fig.4(c) shows the current output of the PSTO15 device at various forces. It can be seen that by keeping the frequency constant at 2 Hz, the current output rises steadily with increasing force. Fig.4(d) shows the long-term stability of the PSTO15 device, confirming that the peak-to-peak voltage amplitude is constant for a longer period. Fig.4(e) shows the load matching analysis; the PSTO15 device voltage increases at various load resistance levels. As per the Ohms law, the voltage should increase as resistance increases, and the same trend is followed. The highest power of the PSTO15 device is measured to be 0.648 μW at 500 MΩ. The switching polarity test was conducted to confirm that the output originated from the PENG in Fig.4(f). The capacitors were charged using PENG and a bridge rectifier. The rectifier circuit helps to convert the AC signal of PENG to the DC signal. Fig.4(g) shows the charging of the capacitors (0.1 and 1 μF) using the PENG. Fig.4(h) shows the charging and discharging of the 0.1 μF capacitor, and the output is stable for a longer period. Fig.4(i) shows the stored charge in the capacitors, which is calculated using the formula $Q = CV$ (where Q=charge, C=capacitance, V=voltage).
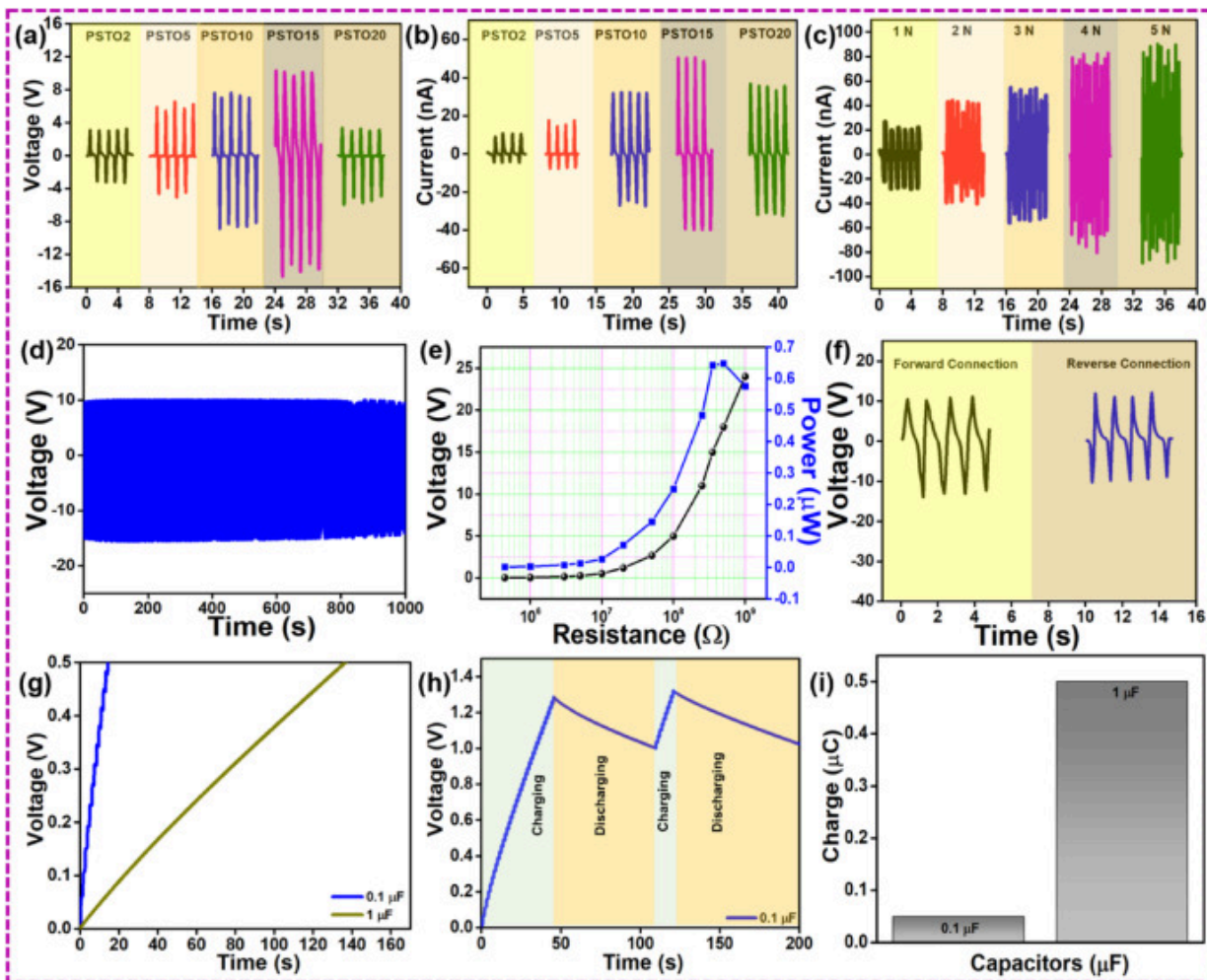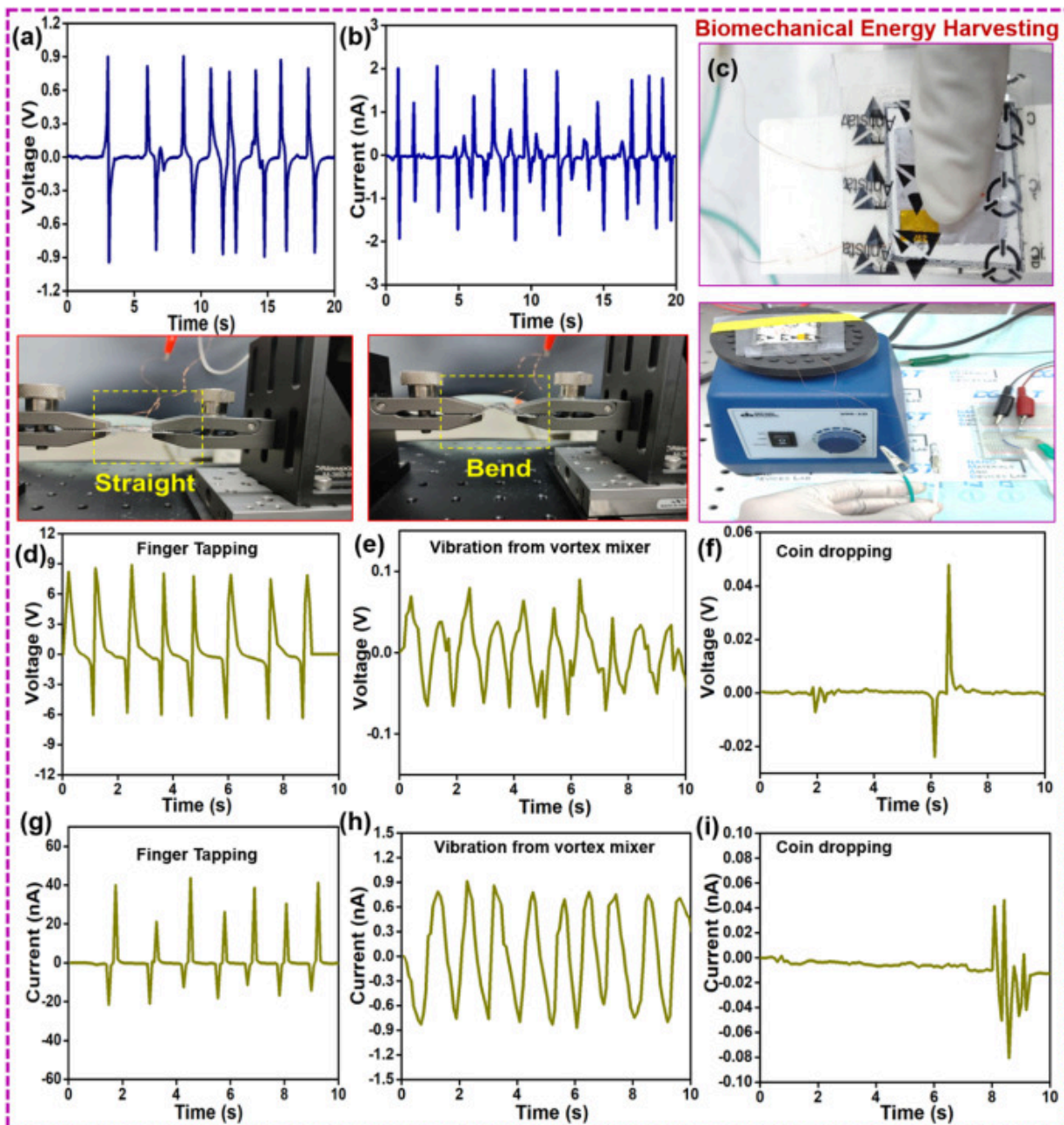

Download: Download high-res image (1MB)
Download: Download full-size image

Fig.4. **Electrical response of the PENG device.** (a–b) voltage and current of different PENG devices made from different mass fraction (%) of STO with PDMS; (c) voltage response of the PSTO15 device at different applied forces; (d) Long-period output stability of the PSTO15 device for 1 000s; (e) power and voltage response of the PSTO15 device at different load resistance; (f) Voltage output of the PSTO15 device using forward and reverse connection (switching polarity test); (g) Charging of capacitors using PSTO15 device; (h) charging and discharging of the 1 μF capacitor and (i) stored charge at various capacitors.

Fig.5(a-b) shows the voltage and current output of the PSTO15 device by bending and releasing. The voltage of 1.8 V and current of 4 nA is generated, confirming that the fabricated PSTO15 device is highly flexible and bendable. Fig.5(c) shows the digital picture of the finger tapping of the PENG, the bending of the PENG, and the PENG attached to a vortex mixture. Fig.5(d–f) show the voltage generated by the PENG under various conditions, such as finger tapping, a vibration of the vortex mixture, and coin dropping. A voltage of 14.4, 0.10 and 0.06 V are generated during finger tapping, a vibration of the vortex mixture, and coin dropping, respectively. A current of 60.00, 0.17 nA, and 0.13 nA are generated during finger tapping, a vibration of vortex mixture, and coin dropping, respectively, as shown in Fig.5(g-i). Hence it can be confirmed that the PENG device can harvest energy from low-frequency vibrations in our daily life.
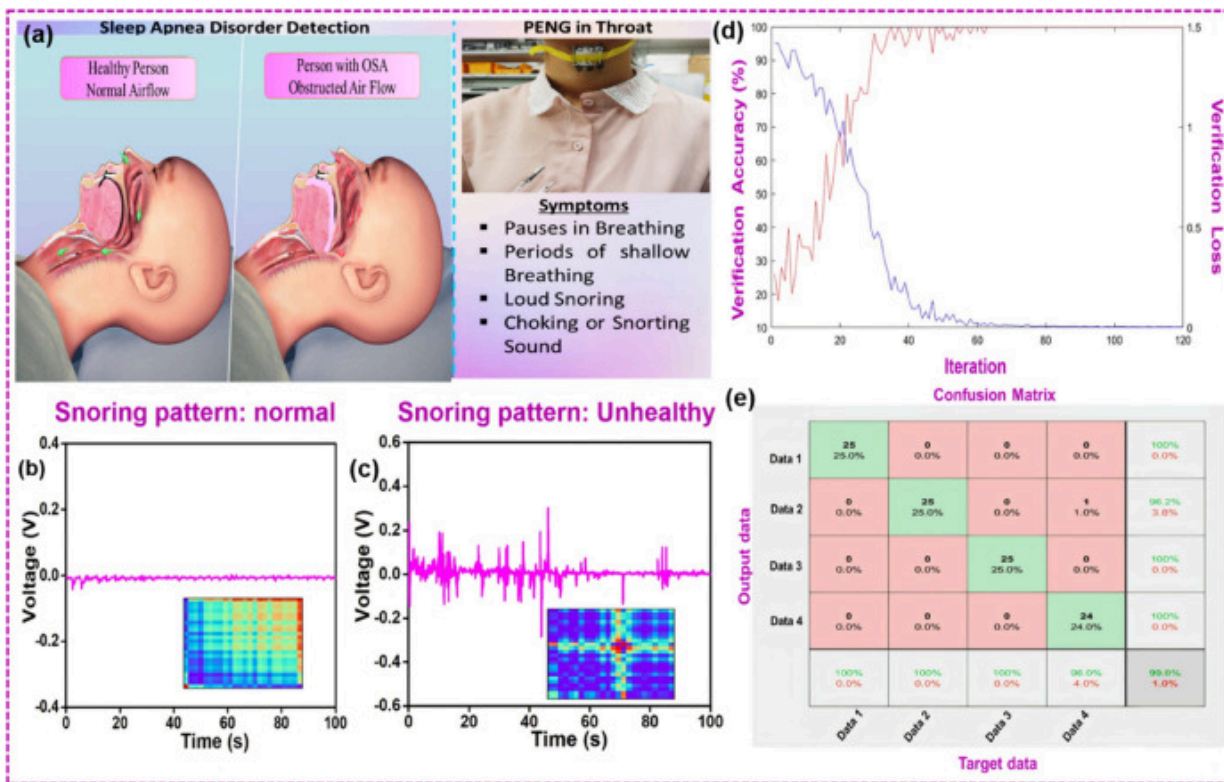

Download: Download high-res image (1MB)
Download: Download full-size image

Fig.5. Biomechanical energy harvesting. (a–b) voltage and current response of the PSTO15 device upon bending; (c) digital image of the PENG device being bent, a finger tapped and attached to the vortex mixer; (d, g) voltage and current output of PSTO15 PENG device upon finger tapping; (e, h)

voltage and current output of PSTO15 PENG device upon vibration from vortex mixer; (f, i) voltage and current output of PSTO15 PENG device upon coin dropping.

Sensor-based healthcare recognition has been gaining interest to improve accuracy and practicality. It has been noted that some of the existing machine learning approaches may perform worse in noisy, non-stationary, and system-uncertain environments, which may result in poor classification due to the possibility of under/overfitting data. As a result, it is necessary to build an effective strategy under these operational conditions. To benefit from CNN's superior performance in image classification, a novel technique that combines GASF and CNN is presented in this study. Fig.6(a) shows a schematic diagram of a healthy person's normal airflow and a person with OSA's obstructive airflow. The PENG was attached to the volunteer's throat larynx area, as shown by a digital picture. The collected outputs had various conditions, such as breathing pauses, periods of shallow breathing, loud snoring, and choking or snorting sounds, as well as the mild snoring pattern of a normal person. The output provided by the PENG was fed to CNN to evaluate the accuracy and effectiveness of identifying the disorder. Several time series signals representing various images resulted in different image feature generation. Each image's input to the CNN model is 200 pixels wide and 200 pixels high. For training, 250 photos from each class are chosen, and the division of this training set is done at random. Each training set includes 100 pictures; 25 photos from each class are used for testing. Fig.6(b and c) show the snoring signal detected from a normal and unhealthy person. In the inset, the GASF image clearly distinguishes a widespread color concentration due to its low magnitude, whereas a loud snoring signal exhibits more color concentration according to its magnitude level. After training, the performance of the proposed system with the produced GASF images appears promising. The accuracy and loss curves of the training procedure are shown in Fig.6(d), and the test set classification results are shown in Fig.6(e). The results show that the overall classification accuracy for test sets of four persons is 99.0%. These outcomes illustrate how well the GASF-CNN system can classify data acquired from various persons. Fig.S5 a, b shows the snoring patterns and corresponding GASF images of two more persons. Using these simple procedures, one can successfully differentiate and diagnose a healthy and unfit individual suffering from OSA. Hence, PENG can act as a cost-effective self-powered sleep monitoring device to identify the fatal OSA disease early and treat the problem for a healthy lifestyle.

Download: Download high-res image (880KB)

Download: Download full-size image

Fig.6. **Self-powered detection of obstructive sleep using convolutional neural network model.** (a) Illustration showing normal breathing and irregular breathing process leading to snoring and symptoms of obstructive sleep; (b, c) voltage response from the PSTO15 PENG device attached to the throat region and the 2D images transferred by using the GASF (inset) of the normal and unhealthy individual; (d) The loss curve and accuracy of the presented GASF-CNN model and (e) Classification results of GASF-CNN.

4. Conclusion

The lead-free polymer-ceramic composites have robust stability and flexibility to act as a base for piezoelectric energy harvesters. STO was synthesized by a mixed oxide route at high temperatures. Further structural, microstructural, and electrical properties of the synthesized material were correlated. STO has orthorhombic symmetry. PDMS-STO composites at different mass fraction of the STO were prepared using a solvent casting route to design and build a PENG. The PSTO15 device gave the highest peak-to-peak voltage, current, and power density of 25V, 92nA, and 0.64μW @ 500MΩ, respectively. Various low-frequency vibrations from daily human motions, bending of the device, and attaching the device to laboratory equipment were utilized to harvest waste energy into useable electrical energy. The snoring signals were recorded by PENG attached to the human throat region. The CNN model help to differentiate between normal and abnormal snores. Such self-powered battery-free sleep monitoring units can help clinicians and patients to analyze their health problems quickly for a healthy life.

Declaration of competing interest

The authors declare that they have no known competing financial interests or personal relationships that could have appeared to influence the work reported in this paper.

Acknowledgement

Appendix A. Supplementary data

The following is the supplementary data to this article:

📄 Download: Download Word document (900KB)
Multimedia component 1.

Recommended articles

References

[1]   A.K. Ng, T.S. Koh, E. Baey, T.H. Lee, U.R. Abeyratne, K. Puvanendran
Could formant frequencies of snore signals be an alternative means for the diagnosis of obstructive sleep apnea?
Sleep Med, 9 (2008), pp. 894-898
📄 View PDF   View article   View in Scopus ↗   Google Scholar ↗

[2]   N. Maimon, P.J. Hanly
Does snoring intensity correlate with the severity of obstructive sleep apnea?
J Clin Sleep Med (2010), pp. 475-478
06
Crossref ↗   View in Scopus ↗   Google Scholar ↗

[3]   A.V. Benjafield, N.T. Ayas, P.R. Eastwood, R. Heinzer, M.S.M. Ip, M.J. Morrell, C.M. Nunez, S.R. Patel, T. Penzel, J.-L. Pépin, P.E. Peppard, S. Sinha, S. Tufik, K. Valentine, A. Malhotra
Estimation of the global prevalence and burden of obstructive sleep apnoea: a literature-based analysis
Lancet Respir Med, 7 (2019), pp. 687-698
📄 View PDF   View article   View in Scopus ↗   Google Scholar ↗

[4]   A.S. Karunajeewa, U.R. Abeyratne, C. Hukins
Multi-feature snore sound analysis in obstructive sleep apnea–hypopnea syndrome
Physiol Meas, 32 (2010), p. 83
Google Scholar ↗

[5]   H. Jin, L.-A. Lee, L. Song, Y. Li, J. Peng, N. Zhong, H.-Y. Li, X. Zhang
Acoustic analysis of snoring in the diagnosis of obstructive sleep apnea syndrome: a call for more rigorous studies
J Clin Sleep Med, 11 (2015), pp. 765-771

Crossref ↗   View in Scopus ↗   Google Scholar ↗

[6]   X. Yang, D. Fan, A. Ren, N. Zhao, S.A. Shah, A. Alomainy, M. Ur-Rehman, Q.H. Abbasi
        Diagnosis of the Hypopnea syndrome in the early stage
        Neural Comput Appl, 32 (3) (2020), pp. 855-866

        Crossref ↗   View in Scopus ↗   Google Scholar ↗

[7]   S.S. Grover, S.D. Pittman
        Automated detection of sleep disordered breathing using a nasal pressure
        monitoring device
        Sleep Breath, 12 (2008), pp. 339-345

        Crossref ↗   View in Scopus ↗   Google Scholar ↗

[8]   H. Li, T. Chang, Y. Gai, K. Liang, Y. Jiao, D. Li, X. Jiang, Y. Wang, X. Huang, H. Wu, Y. Liu, J. Li, Y. Bai, K.
        Geng, N. Zhang, H. Meng, D. Huang, Z. Li, X. Yu, L. Chang
        Human joint enabled flexible self-sustainable sweat sensors
        Nano Energy, 92 (2022), Article 106786

        🗎 View PDF   View article   View in Scopus ↗   Google Scholar ↗

[9]   S. Panda, S. Hajra, K. Mistewicz, P. In-na, M. Sahu, P.M. Rajaitha, H.J. Kim
        Piezoelectric energy harvesting systems for biomedical applications
        Nano Energy, 100 (2022), Article 107514

        🗎 View PDF   View article   View in Scopus ↗   Google Scholar ↗

[10]   G. Rong, Y. Zheng, M. Sawan
        Energy solutions for wearable sensors: a review
        Sensors, 21 (2021), p. 3806

        Crossref ↗   View in Scopus ↗   Google Scholar ↗

[11]   R. Rajagopalan, Y. Tang, X. Ji, C. Jia, H. Wang
        Advancements and challenges in potassium ion batteries: a comprehensive review
        Adv Funct Mater, 30 (2020), Article 1909486

        View in Scopus ↗   Google Scholar ↗

[12]   S.S. Ham, G.J. Lee, D.Y. Hyeon, Y.g. Kim, Y.w. Lim, M.K. Lee, et al.
        Kinetic motion sensors based on flexible and lead-free hybrid piezoelectric
        composite energy harvesters with nanowires-embedded electrodes for detecting
        articular movements
        Compos B Eng, 212 (2021), Article 108705

        🗎 View PDF   View article   View in Scopus ↗   Google Scholar ↗

[13]   T. Quan, Y. Wu, Y. Yang
        Hybrid electromagnetic–triboelectric nanogenerator for harvesting vibration energy
        Nano Res, 8 (2015), pp. 3272-3280

        Crossref ↗   View in Scopus ↗   Google Scholar ↗

[14]   S. Hajra, M. Sahu, A.M. Padhan, I.S. Lee, D.K. Yi, P. Alagarsamy, S.S. Nanda, H.J. Kim
        Agreen metal–organic framework-cyclodextrin MOF: a novel multifunctional
        material based triboelectric nanogenerator for highly efficient mechanical energy

harvesting

Adv Funct Mater, 31 (2021), Article 2101829

View in Scopus ↗   Google Scholar ↗

[15]   S. Hajra, Y. Oh, M. Sahu, K. Lee, H.-G. Kim, B.K. Panigrahi, K. Mistewicz, H.J. Kim
Piezoelectric nanogenerator based on flexible PDMS–BiMgFeCeO6 composites for sound detection and biomechanical energy harvesting

Sustain Energy Fuels, 5 (2021), pp. 6049-6058

Crossref ↗   View in Scopus ↗   Google Scholar ↗

[16]   D.K. Khatua, S.J. Kim
Perspective on the development of high performance flexible piezoelectric energy harvesters

J Mater Chem C, 10 (2022), pp. 2905-2924

Crossref ↗   View in Scopus ↗   Google Scholar ↗

[17]   A.N. Filippin, J.R. Sanchez-Valencia, X. Garcia-Casas, V. Lopez-Flores, M. Macias-Montero, F. Frutos, A. Barranco, A. Borras
3D core-multishell piezoelectric nanogenerators

Nano Energy, 58 (2019), pp. 476-483

📄 View PDF   View article   View in Scopus ↗   Google Scholar ↗

[18]   X. Zhou, K. Parida, O. Halevi, Y. Liu, J. Xiong, S. Magdassi, P.S. Lee
All 3D-printed stretchable piezoelectric nanogenerator with non-protruding kirigami structure

Nano Energy, 72 (2020), Article 104676

📄 View PDF   View article   View in Scopus ↗   Google Scholar ↗

[19]   H. Liu, J. Zhong, C. Lee, S.W. Lee, L. Lin
Acomprehensive review on piezoelectric energy harvesting technology: materials, mechanisms, and applications

Appl Phys Rev, 5 (2018), Article 041306

View in Scopus ↗   Google Scholar ↗

[20]   P. Sharma, S. Hajra, S. Sahoo, P.K. Rout, R.N.P. Choudhary
Structural and electrical characteristics of gallium modified PZT ceramics

Processi Appl Ceram, 11 (2017), pp. 171-176

View in Scopus ↗   Google Scholar ↗

[21]   Y. Zhang, P.T. Thuy Phuong, N.P. Hoang Duy, E. Roake, H. Khanbareh, M. Hopkins, X. Zhou, D. Zhang, K. Zhou, C. Bowen
Polarisation tuneable piezo-catalytic activity of Nb-doped PZT with low Curie temperature for efficient CO_2 reduction and H_2 generation

Nanoscale Adv, 3 (2021), pp. 1362-1374

View article   Crossref ↗   View in Scopus ↗   Google Scholar ↗

[22]   J. Wu
Perovskite lead-free piezoelectric ceramics

J Appl Phys, 127 (2020), Article 190901

Google Scholar ↗

[23]   S. Hajra, A. Tripathy, B.K. Panigrahi, R. Choudhary
Development and excitation performance of lead free electronic material: Eu and Fe
doped $Bi_{0.5}Na_{0.5}TiO_3$ for filter application
Mater Res Express, 6 (2019), Article 076304

Crossref ↗   View in Scopus ↗   Google Scholar ↗

[24]   Y. Zhang, X. Liu, G. Wang, Y. Li, S. Zhang, D. Wang, H. Sun
Enhanced mechanical energy harvesting capability in sodium bismuth titanate
based lead-free piezoelectric
J Alloys Compd, 825 (2020), Article 154020

🗎 View PDF   View article   View in Scopus ↗   Google Scholar ↗

[25]   S. Paramanik, A. Maiti, S. Chatterjee, A.J. Pal
Large resistive switching and artificial synaptic behaviors in layered $Cs_3Sb_2I_9$ lead-
free perovskite memory devices
Adv Electron Mater, 8 (2022), Article 2100237

View in Scopus ↗   Google Scholar ↗

[26]   B.L. Phoon, C.W. Lai, J.C. Juan, P.L. Show, W.H. Chen
Areview of synthesis and morphology of $SrTiO_3$ for energy and other applications
Int J Energy Res, 43 (2019), pp. 5151-5174

Crossref ↗   View in Scopus ↗   Google Scholar ↗

[27]   B. Panda, R. Choudhary
Studies of structural, electrical, and dielectric properties of a new ferroelectric:
$SrTi_2O_5$
J Mater Sci Mater Electron, 3 (2022), pp. 4104-4115

Crossref ↗   View in Scopus ↗   Google Scholar ↗

[28]   Y. Akishige, K. Fukano, H. Shigematsu
New ferroelectric $BaTi_2O_5$, Japanese
J Appl Phys, 42 (2003), pp. L946-L948

View in Scopus ↗   Google Scholar ↗

[29]   Y. Akishige, K. Fukano, H. Shigematsu
New ferroelectric $BaTi_2O_5$
Jpn J Appl Phys, 42 (2003), p. L946

View in Scopus ↗   Google Scholar ↗

[30]   T. Kimura, T. Goto, H. Yamane, H. Iwata, T. Kajiwara, T. Akashi
Aferroelectric barium titanate, $BaTi_2O_5$
Acta Crystallogr Sect C Cryst Struct Commun, 59 (2003), pp. i128-i130

View in Scopus ↗   Google Scholar ↗

[31]   P. Fisher, H. Du, M. Skowronski, P. Salvador, O. Maksimov, X. Weng

Stoichiometric, nonstoichiometric, and locally nonstoichiometric $SrTiO_3$ films grown by molecular beam epitaxy

J Appl Phys, 103 (2008), Article 013519

View in Scopus ↗ Google Scholar ↗

[32] B. Dudem, L.K. Bharat, H. Patnam, A.R. Mule, J.S. Yu

Enhancing the output performance of hybrid nanogenerators based on Al-doped $BaTiO_3$ composite films: a self-powered utility system for portable electronics

J Mater Chem, 6 (2018), pp. 16101-16110

Crossref ↗ View in Scopus ↗ Google Scholar ↗

[33] H. Patnam, B. Dudem, N.R. Alluri, A.R. Mule, S.A. Graham, S.J. Kim, *et al.*

Piezo/triboelectric hybrid nanogenerators based on Ca-doped barium zirconate titanate embedded composite polymers for wearable electronics

Compos Sci Technol, 188 (2020), Article 107963

View PDF View article View in Scopus ↗ Google Scholar ↗

[34] Y. Yu, Z. Li, Y. Wang, S. Gong, X. Wang

Sequential infiltration synthesis of doped polymer films with tunable electrical properties for efficient triboelectric nanogenerator development

Adv Mater, 27 (2015), pp. 4938-4944

Crossref ↗ View in Scopus ↗ Google Scholar ↗

[35] M.M. Alam, D. Mandal

Native cellulose microfiber-based hybrid piezoelectric generator for mechanical energy harvesting utility

ACS Appl Mater Interfaces, 8 (2016), pp. 1555-1558

Crossref ↗ View in Scopus ↗ Google Scholar ↗

[36] T. Song, J. Kim, S.I. Kwun, C. Kim, J.J. Kim

Raman spectroscopy of quantum paraelectric $SrTiO_3$ fine particles

Phys B Condens Matter, 219 (1996), pp. 538-540

View PDF View article View in Scopus ↗ Google Scholar ↗

[37] R. Migoni, K. Rieder, K. Fischer, H. Bilz

Lattice dynamics and Raman spectra of SrTiO3

Ferroelectrics, 13 (1976), pp. 377-379

Crossref ↗ View in Scopus ↗ Google Scholar ↗

[38] D.A. Tenne, A. Farrar, C. Brooks, T. Heeg, J. Schubert, H. Jang, C. Bark, C. Folkman, C. Eom, D. Schlom

Ferroelectricity in nonstoichiometric $SrTiO_3$ films studied by ultraviolet Raman spectroscopy

Appl Phys Lett, 97 (2010), Article 142901

View in Scopus ↗ Google Scholar ↗

[39] M. El-Desoky, I. Morad, M. Wasfy, A. Mansour

Synthesis, structural and electrical properties of PVA/TiO_2 nanocomposite films with different TiO_2 phases prepared by sol–gel technique

J Mater Sci Mater Electron, 31 (2020), pp. 17574-17584

Crossref ↗   View in Scopus ↗   Google Scholar ↗

[40]   S. Hejabri Kandeh, S. Amini, H. Ebrahimzadeh
Simultaneous trace-level monitoring of seven opioid analgesic drugs in biological samples by pipette-tip micro solid phase extraction based on PVA-PAA/CNT-CNC composite nanofibers followed by HPLC-UV analysis
Microchim Acta, 188 (2021), pp. 1-10

Google Scholar ↗

[41]   B. Kisan, J. Kumar, A.M. Padhan, P. Alagarsamy, D. Pamu
Size and strain induced phase formation and ferromagnetism in reduced TiO_2 powders
J Phys Chem Solid, 154 (2021), Article 110058

🔴 View PDF   View article   View in Scopus ↗   Google Scholar ↗

[42]   R. Panigrahi, S. Hajra, M. De, A. Kumar, A. James, R. Choudhary
Investigation of resistive, capacitive and conductive properties of lead-free electronic material: $0.7Bi(FeO_{0.98}Ga_{0.02})O_3$-$0.30\ BaTiO_3$
Solid State Sci, 92 (2019), pp. 6-12

🔴 View PDF   View article   View in Scopus ↗   Google Scholar ↗

[43]   P. Gupta, P.K. Mahapatra, R.N.P. Choudhary
Structural and electrical characteristics of rare-earth modified bismuth layer structured compounds
J Alloys Compd, 863 (2021), Article 158457

🔴 View PDF   View article   View in Scopus ↗   Google Scholar ↗

[44]   K. Auromun, R.N.P. Choudhary
Structural, dielectric, and electrical characteristics of selenium-modified $BiFeO_3$–$(BaSr)TiO_3$ ceramics
J Mater Sci Mater Electron, 31 (2020), pp. 13415-13433

Crossref ↗   View in Scopus ↗   Google Scholar ↗

[45]   S.K. Patri, P.L. Deepti, R.N.P. Choudhary, B. Behera
Dielectric, impedance and modulus spectroscopy of $BaBi_2Nb_2O_9$
J Electroceram, 40 (2018), pp. 338-346

Crossref ↗   View in Scopus ↗   Google Scholar ↗

[46]   M.Z. Iqbal
Rafiuddin, Structural, electrical conductivity and dielectric behavior of Na_2SO_4–LDT composite solid electrolyte
J Adv Res, 7 (2016), pp. 135-141

🔴 View PDF   View article   View in Scopus ↗   Google Scholar ↗

[47]   N.R. Alluri, A. Chandrasekhar, S.J. Kim
Exalted electric output *via* piezoelectric–triboelectric coupling/sustainable butterfly wing structure type multiunit hybrid nanogenerator

ACS Sustainable Chem Eng, 6 (2018), pp. 1919-1933

Crossref ↗   View in Scopus ↗   Google Scholar ↗

Cited by (21)

3D vertically aligned microchannel structure to enhance piezoelectric energy harvesting performance of PZT/PVDF&CNTs piezoelectric composites

2024, Journal of Materiomics

Show abstract ⌄

Hybrid nanogenerator for self-powered object recognition

2024, Journal of Science: Advanced Materials and Devices

> *Citation Excerpt :*
>
> …For example, Convolutional Neural Network (CNN) has been integrated with machine learning to improve object recognition capabilities and enable sensors to understand object interactions and properties. The ability of a sensor developed using hybrid energy harvesting technology and CNN to accurately detect, classify, or predict events or circumstances relative to real-world or predicted outcomes is called accuracy [20,35]. A higher level of accuracy indicates that the sensor system, powered by energy harvesting and supported by CNN, is more reliable and useful in its intended application, while a lower accuracy indicates that the system design or machine learning algorithms need to be improved or refined.…

Show abstract ⌄

Enhancing structural response via macro-micro hierarchy for piezoelectric nanogenerator and self-powered wearable controller

2024, Chemical Engineering Journal

> *Citation Excerpt :*
>
> …Piezoelectric polymer composites (PPC) characterized by piezoelectricity, flexibility and easy processability present a promising solution as a self-powered source for flexible electronic devices[12–15]. These composites can efficiently convert high-entropy energy, such as vibration and impact, into electricity, enabling the performance of both sensing and actuation functions[16–19]. However, the majority of research has primarily concentrated on PPC films or fibers, neglecting to fully exploit the advantages of normal deformation[20–23].…

Show abstract ⌄

Piezoelectric Biomaterials Inspired by Nature for Applications in Biomedicine and Nanotechnology ↗

2024, Advanced Materials

Pyroelectric based energy harvesting devices: hybrid structures and applications ↗

2023, Sustainable Energy and Fuels

Zinc Ferrite Nanoparticle-Based Wearable Piezoelectric Nanogenerators as Self-Powered Sensors to Monitor Human Motion ↗

2023, ACS Applied Nano Materials

> View all citing articles on Scopus ↗

Ms. Swati Panda is currently a doctoral student at Daegu Gyeongbuk Institute of Science and Technology. She received her Bachelor's degree from Utkal University, Orissa in 2018. She pursued her Master's degree from Siksha 'O' Anusandhan University with a specialization in biotechnology in 2020. Her research interests focus on self-powered biosensors and piezoelectric energy harvesters.

Dr. Hoe Joon Kim is currently an Associate Professor in Robotics Engineering with the Daegu Gyeongbuk Institute of Science and Technology (DGST), Daegu, South Korea, and also holds a courtesy appointment in the Information and Communication Engineering Department. He received the B.S. degree from Johns Hopkins University, Baltimore, MD, USA, in 2009, and the M. S. and Ph. D. degrees from the University of Illinois at Urbana–Champaign, Urbana, IL, USA, in 2011 and 2015, respectively, all in mechanical engineering. He held a post-doctoral position at the Micro and Nano Systems Laboratory, Carnegie Mellon University, Pittsburgh, PA, USA, where he was involved in the development of low-power low-noise piezoelectric MEMS resonators for sensing and frequency control applications. His research interests focus on piezoelectric MEMS resonators for RF wireless communication, chemical/physical sensing, environmental monitoring and emerging nanomaterials.

Peer review under responsibility of The Chinese Ceramic Society.

ELSEVIER

RELX™